processes

MDPI

Article

Model-Free Adaptive Sliding Mode Control Scheme Based on DESO and Its Automation Application

Xiaohua Wei [1], Zhen Sui [2,*], Hanzhou Peng [3], Feng Xu [1,2], Jianliang Xu [1] and Yulong Wang [4,*]

[1] School of Mechanical and Electrical Engineering, Quzhou College of Technology, Quzhou 324000, China; wxhqct@yeah.net (X.W.); fengxu15@mails.jlu.edu.cn (F.X.); xujianliang84@gmail.com (J.X.)
[2] College of Communication Engineering, Jilin University, Changchun 130022, China
[3] China Railway Guangzhou Group Co., Ltd. Changsha Electric Service Depot, Changsha 410001, China; 15866628622@163.com
[4] Quzhou Special Equipment Inspection & Testing Research Institute, Quzhou 324000, China
* Correspondence: suizhen@jlu.edu.cn (Z.S.); wyl125739@163.com (Y.W.)

Abstract: This paper addresses a class of uncertain nonlinear systems with disturbances that are challenging to model by proposing a novel model-free adaptive sliding mode control (MFASMC) scheme based on a discrete-time extended state observer (DESO). Initially, leveraging the pseudo partial derivative (PPD) concept in the model-free adaptive control (MFAC) framework, the discrete-time nonlinear model is converted into a full-form dynamic linearization (FFDL) model. Secondly, using the FFDL data model, a discrete sliding mode controller is designed. A discrete integral sliding mode surface is chosen to mitigate chattering during the reaching phase, and a hyperbolic tangent function with minimal slope variation is selected for smoother switching control. Furthermore, a DESO is designed to estimate uncertainties in the discrete system, enabling real-time compensation for the controller. Finally, a genetic optimization algorithm is employed for parameter tuning to minimize the time cost associated with selecting control parameters. The design process of this scheme relies solely on the data of the controlled system, without depending on a mathematical model. The proposed DESO-MFASMC scheme is tested through simulations using a typical numerical equation and the existing EFG-BC/320 electric heavy-duty forklift from the Quzhou Special Equipment Inspection Center. Simulation results show that the proposed method is significantly superior to the traditional MFAC and PID control methods in tracking accuracy and robustness when dealing with nonlinear disturbance of the system. The DESO-MFASMC scheme proposed in this paper not only shows its advantages in theory but also verifies its effectiveness and practicability in engineering through practical application.

Keywords: sliding mode control (SMC); full-form dynamic linearization (FFDL); model-free adaptive control (MFAC); genetic algorithm (GA); discrete-time extended state observer (DESO); electric heavy-duty forklift

Citation: Wei, X.; Sui, Z.; Peng, H.; Xu, F.; Xu, J.; Wang, Y. Model-Free Adaptive Sliding Mode Control Scheme Based on DESO and Its Automation Application. *Processes* **2024**, *12*, 1950. https://doi.org/10.3390/pr12091950

Academic Editor: Mohd Azlan Hussain

Received: 19 July 2024
Revised: 18 August 2024
Accepted: 9 September 2024
Published: 11 September 2024

1. Introduction

In recent years, with the continuous advancement of automation across various industries, the demand for control precision in systems has been increasing. The control problem of discrete-time nonlinear systems, which are difficult to model due to uncertainties and disturbances, has gradually become a prominent and challenging topic in academic research. SMC, a nonlinear robust control strategy, is known for its ease of implementation and high robustness in the presence of disturbances [1]. It has been extensively studied and successfully applied to many practical systems, such as robotic arm posture control systems [2,3], train operation systems [4,5], and boiler water-level control systems [6,7]. Theoretically, equivalent SMC only exists in ideal continuous SMC, while for discrete systems, only quasi-sliding mode control is possible. Additionally, due to the presence of the sampling period in digital control, directly applying continuous-time SMC algorithms to

discrete-time systems can lead to several issues, such as significant chattering, discretization errors, and even system instability [8,9]. Therefore, to achieve high-performance variable structure control in sampled data systems, it is preferable to select discrete-time SMC (DSMC) algorithms [10–12].

In DSMC, chattering between positive and negative outputs, as well as unmodeled dynamics, have become bottlenecks limiting its development. To address the chattering problem in DSMC, many researchers have combined DSMC with other control algorithms to form new control systems that suppress or eliminate chattering disturbances. Refs. [13,14] proposed a discrete terminal SMC (DTSMC) method, which can make the discrete sliding mode system respond faster and converge within a finite time by adjusting the parameters of the DTSMC. Studies have shown that DSMC with an integral sliding mode surface can provide better control performance than the traditional sliding mode surface [15,16]. Refs. [17,18] introduced discrete integral terminal SMC (DITSMC), which uses fractional power rules to achieve a nonlinear manifold. Once the sliding surface is reached, this enables faster convergence of the system state and has been successfully applied to micro/nano positioning and piezoelectric-driven motion systems. Ref. [19] designed a fast terminal sliding mode controller with output constraints; this could achieve the desired state in a shorter time by adjusting parameters, eliminating the chattering of SMC, but did not solve the singularity problem in terminal sliding mode. Ref. [20] first applied the least squares method to identify the corresponding linear model, designed the train operation target curve according to the train operation requirements and energy-saving optimization theory, and finally, designed a sliding mode predictive controller. By using the pole placement method, an asymptotically stable sliding mode surface was designed, effectively overcoming the chattering phenomenon, although lacking theoretical proof. All the aforementioned methods require a known mathematical model. However, the process of establishing a reliable model for systems is very burdensome and challenging.

Fortunately, Ref. [21] proposed a non-parametric dynamic linearization method, a model-free approach for discrete nonlinear system modeling based on the concept of PPD. The acquisition of PPD relies solely on system input and output data, and the design of the controller also depends solely on these data. This method offers a viable solution to the challenging problem of nonlinear system modeling. Ref. [22] introduced an MFASMC method based on an exponential reaching law. However, this approach requires improvements in response time and tracking accuracy. Building upon this work, Ref. [23] utilized a radial basis function neural network estimator to comprehensively estimate system uncertainties and proposed a network-adaptive SMC law based on precise data models, achieving enhanced control performance. Ref. [24] developed an MFASMC for an exoskeleton robot. Ref. [25] presented an enhanced MFAC method incorporating a disturbance observer. Expanding on these approaches, Ref. [26] integrated the non-parametric dynamic linearization method with observer concepts to achieve real-time dynamic linearization of systems with disturbances, thus extending the applicability of MFAC to a broader range of discrete systems. Ref. [27] applied higher-order SMC concepts and introduced a second-order quasi-sliding mode MFAC method for systems with disturbances. Addressing actuator faults in subway trains, Ref. [28] proposed a fault-tolerant MFASMC, considering system I/O constraints to enhance subway train operation safety. Finally, Ref. [29] introduced an improved partial format MFASMC method, which integrates energy consumption considerations into control force design, trading some control accuracy for reduced energy usage. Ref. [30] proposed a model-free adaptive quasi-sliding mode control method based on dynamic linearization and a predefined performance function. However, this approach does not consider the impact of uncertainties, such as disturbances in actual systems. In [31], the authors applied a data-driven sliding mode control to the attitude control of a robot and addressed the poor disturbance rejection capability of traditional MFAC. However, this approach introduced adverse effects such as chattering from the DSMC, which needs to be further addressed in future studies. Refs. [32,33] combined the advantages of the MFAC and DSMC methods to design a composite controller, where the MFAC method reduced the controller's reliance

on the system model information, while the DSMC method compensated for the effects of unknown external disturbances and unmodeled dynamics. However, it is difficult to guarantee the convergence of the composite controller. It is noteworthy that the dynamic linearization method offers advantages to DSMC in that it does not depend on the model, but it does not solve the problem that DSMC requires a large switching gain to handle interference, and the switch action will produce chattering and other problems that affect performance. To address these challenges, Ref. [34] designed a data-driven integral sliding mode control method combined with an extended state observer (ESO) to compensate for unknown terms, thereby achieving the control objectives of suppressing chattering and providing disturbance rejection. However, research results indicated that the introduction of ESO in MFAC and data-driven sliding mode control methods, as shown in [35], restricts the flexibility in selecting data models and requires stringent assumptions for the convergence proof process.

Based on the above analysis, in this paper, a new MFASMC algorithm based on a DESO is proposed for nonlinear discrete-time systems with disturbances. Firstly, the pseudo-gradient concept in the MFAC framework is used to transform the discrete-time nonlinear Model into an FFDL data model. Secondly, a discrete sliding mode controller is designed using the FFDL data model, a discrete integral sliding mode surface is selected to eliminate buffeting at the arrival stage of the sliding mode, and a hyperbolic tangent function with small slope change is selected for switching control to make the switching smoother. A DESO is further designed to estimate the uncertainties in the discrete system to achieve real-time compensation of the controller. Finally, in order to reduce the time cost of control parameter selection, a genetic optimization algorithm is used to adjust the parameters. The design process of the scheme only needs to use the input and output data of the controlled system, without relying on a mathematical model. The proposed DESO-MFASMC method is simulated and tested on a forklift and compared with traditional methods. The simulation results validate the effectiveness and superiority of the DESO-MFASMC. The main contributions of this paper are as follows: (1) This paper aims at multi-input multiple-output discrete-time systems, and the multi-input multiple-output control algorithm increases the difficulty of selecting control parameters. Therefore, a genetic algorithm is introduced to adjust the controller parameters by the principle of survival of the fittest to reduce the time cost of parameter selection. (2) Compared with tight-format dynamic linearization and partial-format dynamic linearization, the FFDL method used in this paper fully utilized the relationship between input change and output change. The system has more adjustable degrees of freedom and greater design flexibility. (3) Compared with [36], this paper adopts integral sliding mode control on the basis of model-free adaptive sliding mode control to reduce the buffeting problem caused by ordinary sliding mode surface, improve the stability of the controller, and make the control accuracy higher. (4) Compared with [37], the discrete extended state observer is introduced in the controller design for real-time compensation to reduce the influence of external disturbances on the control effect, which is more consistent with the real system operating environment. (5) Compared with the MFAC method used in [22,23], this paper further introduces a discrete sliding mode control algorithm to reduce the influence of measurement perturbations. In order to prevent the output from being too large, a parameter estimation error is introduced as a limiting term to improve the robustness of the system. (6) Compared with [3,4], the proposed algorithm does not depend on the dynamic model of the system and is a data-driven control algorithm.

2. Dynamic Linearization Method and DESO

2.1. Dynamic Linearization

Considering the inherent uncertainties of complex controlled systems and the various interferences encountered in operational environments, establishing precise mathematical models for such systems is challenging. To monitor the operational status of the system, data acquisition devices are typically integrated within the system. Taking an electric

counterbalanced forklift as an example, its chassis is equipped with components such as speed sensors, position sensors, and transponders. During operation, these sensors collect comprehensive I/O data. In summary, a general nonlinear non-affine system can be represented as the following data set:

$$\mathbf{v}(s+1)=f(\mathbf{v}(s),\ldots,\mathbf{v}(s-p_v),\mathbf{u}(s),\ldots,\mathbf{u}(s-p_u),\mathbf{d}(s),\ldots,\mathbf{d}(s-p_d)) \tag{1}$$

where $\mathbf{v}(s) = [v_1(s),\cdots,v_i(s),\cdots,v_n(s)]^{\mathrm{T}}$ and $\mathbf{u}(s) = [u_1(s),\cdots,u_i(s),\cdots,u_n(s)]^{\mathrm{T}}$ are the total output and total input of the system, respectively; s is the sampling time of the discrete system; $\mathbf{d}(s)= [d_1(s),\cdots,d_i(s),\cdots,d_n(s)]^{\mathrm{T}}$ represents the disturbance experienced by the controlled system during operation; and p_v, p_u, and p_d are unknown positive integers related to the output, input, and disturbance terms, respectively.

Define $\mathbf{H}(s) \in R^{L_v+L_u}$ as

$$\mathbf{H}(s) = [\mathbf{v}^{\mathrm{T}}(s),\cdots,\mathbf{v}^{\mathrm{T}}(s-L_v+1),\mathbf{u}^{\mathrm{T}}(s),\cdots,\mathbf{u}^{\mathrm{T}}(s-L_u+1)]^{\mathrm{T}} \tag{2}$$

where $L_v(0 \le L_v \le n_v)$ is called the linearization length constant of the discrete system output and $L_u(0 \le L_u \le n_u)$ is called the linearization length constant of the discrete system input.

Remark 1. *Owing to the uncertainty in* $\mathbf{d}(s)$ *experienced by the controlled system during operation* $\mathbf{d}(s)$*, to avoid significant parameter variations and increase computational complexity when linearizing model (1), the disturbance term is not included in the variable* $\mathbf{H}(s)$ *selection, but is considered separately.*

Assumption 1. $f(\cdot)$ *is continuously differentiable with respect to all variables in system (1).*

Assumption 2. *The system satisfies the generalized Lipschitz condition, that is, for* $s_1 \neq s_2$ *and* $s_1, s_2 \ge 0$*, there exist:*

$$\|\mathbf{v}(s_1+1)-\mathbf{v}(s_2+1)\| \le b_0\|\mathbf{H}(s_1)-\mathbf{H}(s_2)\| \tag{3}$$

where $\mathbf{v}(s_j+1) = f(\mathbf{v}(s_j),\cdots,\mathbf{v}(s_j-L_y),\mathbf{u}(s_j),\cdots,\mathbf{u}(s_j-L_u),\mathbf{d}(s_j),\cdots,\mathbf{d}(s_j-L_d))$*; and* $b_0 > 0$ *is a constant.*

Theorem 1. *For a nonlinear system (1), there exists a time-varying matrix* $\mathbf{\Phi}(s) \in R^{L_v+L_u}$*, with* $0 \le L_v \le n_v$ *and* $1 \le L_u \le n_u$*, such that*

$$\Delta\mathbf{v}(s+1) = \mathbf{\Phi}^{\mathrm{T}}(s)\Delta\mathbf{H}(s) \tag{4}$$

where $\mathbf{\Phi}(s) = [\Phi_1(s),\cdots,\Phi_{L_v}(s),\cdots,\Phi_{L_v+L_u}(s)]^{\mathrm{T}} \in R^{n\times(nL_v+nL_u)}$ *and* $\Phi_l(s) \in R^{n\times n}$ *is the corresponding submatrix.*

Proof. See Appendix A for details. □

The following assumption is made for the parameter matrix $\mathbf{\Phi}(s)$ to ensure the strictness of the control system design.

Assumption 3. $\Phi_{L_v+1}(s)$ *is a diagonal-dominant matrix, i.e., it satisfies* $\left|\phi_{ijl}(s)\right| \le b_1$*,* $b_2 \le |\phi_{iil}(s)| \le \alpha b_2$*,* $\alpha \ge 1$*, and* $b_2 > b_1(2\alpha+1)(n-1)$*, the signs of all elements remain unchanged at all times.*

For the unknown PPJM in the dynamic linearized data model (4), the following PPJM matrix estimation function is considered:

$$J(\mathbf{\Phi}(s)) = \left\|\Delta\mathbf{v}(s)-\mathbf{\Phi}^{\mathrm{T}}(s)\Delta\mathbf{H}(s-1)\right\|^2+\mu\left\|\mathbf{\Phi}(s)-\hat{\mathbf{\Phi}}(s-1)\right\|^2 \tag{5}$$

where μ is a constant and $\hat{\mathbf{\Phi}}(s)$ represents the estimated value of $\mathbf{\Phi}(s)$.

Taking the extremum of $\mathbf{\Phi}(s)$ in Equation (5), we obtain the estimation algorithm:

$$\hat{\mathbf{\Phi}}(s) = \hat{\mathbf{\Phi}}(s-1) + \frac{\eta \Delta \mathbf{v}(s) \Delta \mathbf{H}^{\mathrm{T}}(s-1)}{\mu + \|\Delta \mathbf{H}(s-1)\|^2} - \frac{\eta \hat{\mathbf{\Phi}}(s-1) \Delta \mathbf{H}(s-1) \Delta \mathbf{H}^{\mathrm{T}}(s-1)}{\mu + \|\Delta \mathbf{H}(s-1)\|^2} \tag{6}$$

where $\eta \in (0,2]$; $\hat{\mathbf{\Phi}}(s) = [\hat{\Phi}_1(s), \cdots, \hat{\Phi}_{L_v}(s), \cdots, \hat{\Phi}_{L_v+L_u}(s)]^{\mathrm{T}} \in R^{n \times (nL_v + nL_u)}$, and $\hat{\Phi}_l(s) \in R^{n \times n}$ is the estimated value of the corresponding submatrix.

The algorithm reset mechanism (7) and (8) is introduced.

$$\begin{array}{l} \hat{\phi}_{ii(L_v+1)}(s) = \hat{\phi}_{ii(L_v+1)}(1) \\ \text{if } \left|\hat{\phi}_{ii(L_v+1)}(s)\right| < b_2 \text{ or } \left|\hat{\phi}_{ii(L_v+1)}(s)\right| > \alpha b_2 \\ \text{orsign}(\hat{\phi}_{ii(L_v+1)}(s)) \neq \text{sign}(\hat{\phi}_{ii(L_v+1)}(1)),\ i = 1, \cdots, n \end{array} \tag{7}$$

$$\begin{array}{l} \hat{\phi}_{ij(L_v+1)}(s) = \hat{\phi}_{ij(L_v+1)}(1) \\ \text{if } \left|\hat{\phi}_{ij(L_v+1)}(s)\right| > b_1 \text{ or} \\ \text{sign}(\hat{\phi}_{ij(L_v+1)}(s)) \neq \text{sign}(\hat{\phi}_{ij(L_v+1)}(1)), i \neq j \end{array} \tag{8}$$

where $\hat{\phi}_{ii(L_v+1)}(s)$ is the diagonal element in $\hat{\Phi}_{L_v+1}$; $\hat{\phi}_{ii(L_v+1)}(1)$ is the initial value of $\hat{\phi}_{ii(L_v+1)}(s)$; and $\hat{\phi}_{ij(L_v+1)}(s)$ is an off-diagonal element in $\hat{\Phi}_{L_v+1}$.

2.2. DESO Design

Due to the nonlinear terms in $\mathbf{\Phi}(s)$ and potential unknown disturbances during system operation, $\hat{\mathbf{\Phi}}(s)$ experiences significant fluctuations, rendering it unsuitable for predict the true value of $\mathbf{\Phi}(s)$. Consequently, define $\mathbf{J}(s) = \tilde{\mathbf{\Phi}}^{\mathrm{T}}(s) \Delta \mathbf{H}(s)$, where $\tilde{\mathbf{\Phi}}(s) = \mathbf{\Phi}(s) - \hat{\mathbf{\Phi}}(s)$ represents the estimation error of the time-varying PPJM.

By using the characteristics of DESO that can observe and compensate the states and unknown disturbances of the system, $\mathbf{J}(s)$ is extended to a state variable, and $\mathbf{J}(s)$ is approximated by a linear function to reduce the influence of the integration term on the control effect. Therefore, Equation (4) can be written as

$$\Delta \mathbf{v}(s+1) = \hat{\mathbf{\Phi}}^{\mathrm{T}}(s) \Delta \mathbf{H}(s) + \mathbf{J}(s) \tag{9}$$

DESO is a tool used in control systems to estimate system states and disturbances, often in adaptive control and robust control fields. By extending the state space of the system to estimate both the state variables and the unknown disturbance, it improves the control performance and anti-interference ability of the system. The core idea is to treat the unknown disturbance of the system as part of the extended state, and to estimate the state and disturbance of the system simultaneously by designing an observer. Based on the dynamic linearized data model, the extended state observer is used to observe and compensate each state of the system and the unknown disturbance. The unknown term is extended to a state variable, and the linear function alignment is used to approximate, which reduces the influence of the integrated unknown term control effect. DESO can be represented in the following form:

$$\begin{cases} \mathbf{v}_m(s+1) = \mathbf{v}_m(s) + \hat{\mathbf{\Phi}}^{\mathrm{T}}(s) \Delta \mathbf{H}(s) + \hat{\mathbf{J}}(s) + l_1(\mathbf{v}(s) - \mathbf{v}_m(s)) \\ \hat{\mathbf{J}}(s) = \hat{\mathbf{J}}(s-1) + l_2(\mathbf{v}(s) - \mathbf{v}_m(s)) \end{cases} \tag{10}$$

where $\mathbf{v}_m(s) = [v_{m1}(s), \cdots, v_{mn}(s)]^{\mathrm{T}}$; $\hat{\mathbf{J}}(s) = [\hat{J}_1(s), \cdots, \hat{J}_n(s)]$; and l_1 and l_2 denote the observer gain.

To ensure the boundedness of the DESO compensation range, $\hat{\mathbf{J}}(s)$ must satisfy a saturation function:

$$\hat{J}_i(s) = \begin{cases} J_0 \hat{J}_i(s) > J_0 \\ \hat{J}(s) - J_0 < \hat{J}_i(s) < J_0 \\ -J_0 \hat{J}_i(s) < -J_0 \end{cases} \tag{11}$$

where $J_0 > 0$ is the constant of the saturation function.

3. DESO-MFASMC Design

3.1. Sliding Mode Surface Design

The error $\mathbf{e}(s)$ of the controlled system at time instant s is defined as:

$$\mathbf{e}(s) = \mathbf{v}_d(s) - \mathbf{v}(s) \tag{12}$$

where $\mathbf{e}(s) = [e_1(s), \cdots, e_n(s)]$ and $\mathbf{v}_d(s) = [v_{d1}(s), \cdots, v_{dn}(s)]$ is the bounded expected output.

To improve the stability of sliding mode motion, the following function is designed:

$$\mathbf{\Psi}(s+1) = \mathbf{e}(s{+}1) + h \sum_{i=1}^{s+1} T\mathbf{e}(s) \tag{13}$$

where $\mathbf{\Psi}(s) = [\Psi_1(s), \cdots, \Psi_n(s)]$; T denotes the sampling time; and h is a constant.

3.2. DESO-MFASMC Law Design

The control law design for DESO-MFASMC consists of two components. $\mathbf{u}_{eq}$ represents the equivalent control part and $\mathbf{u}_{sw}$ denotes the switching control part, an additional discontinuous term introduced to enhance the robustness of the controller and mitigate chattering in the system.

$$\mathbf{u}(s) = \mathbf{u}(s-1) + \mathbf{u}_{eq}(s) + \mathbf{u}_{sw}(s) \tag{14}$$

The equivalent control input $\mathbf{u}_{eq}$ for the DESO-MFASMC is obtained using Equation (15).

$$\mathbf{\Psi}(k+1) - \mathbf{\Psi}(k) = 0 \tag{15}$$

Inserting Equation (13) into Equation (15), we obtain:

$$\Delta\mathbf{\Psi}(s+1) = (1+hT)\mathbf{e}(s{+}1) - \mathbf{e}(s) \tag{16}$$

Setting Equation (16) to zero and substituting Equations (6) and (10), we obtain the equivalent control law $\mathbf{u}_{eq}$.

$$\begin{aligned} \mathbf{u}_{eq}(s) = {} & \frac{\rho_1 \hat{\mathbf{\Phi}}_{L_v+1}(s)}{\left\|\hat{\mathbf{\Phi}}_{L_v+1}(s)\right\|^2+\sigma}\left(\mathbf{v}_d(s+1) - \mathbf{v}(s) - \hat{\mathbf{J}}(s)\right) - \frac{\hat{\mathbf{\Phi}}_{L_v+1}(s)}{\left\|\hat{\mathbf{\Phi}}_{L_v+1}(s)\right\|^2+\sigma}\Big(\sum_{i=1}^{L_v} \rho_{i+1}\hat{\mathbf{\Phi}}_i^{\mathrm{T}}(s)\Delta\mathbf{v}(s-i+1)\Big) \\ & - \frac{\hat{\mathbf{\Phi}}_{L_v+1}(s)}{\left\|\hat{\mathbf{\Phi}}_{L_v+1}(s)\right\|^2+\sigma}\Big(\sum_{j=L_v+2}^{L_v+L_u} \rho_j\hat{\mathbf{\Phi}}_j^{\mathrm{T}}(s)\Delta\mathbf{u}(s-L_v-j+1)\Big) - \frac{\hat{\mathbf{\Phi}}_{L_v+1}(s)}{\left\|\hat{\mathbf{\Phi}}_{L_v+1}(s)\right\|^2+\sigma} \times \frac{\mathbf{e}(s)}{1+hT} \end{aligned} \tag{17}$$

where σ denotes a constant introduced to prevent the denominator from becoming zero.

In terms of switching control laws, the hyperbolic tangent function exhibits superior performance in suppressing chattering compared to conventional sign functions, resulting in the switched control law as expressed in Equation (18).

$$\mathbf{u}_{sw}(s) = w_s \times \tanh(\mathbf{\Psi}(s)) \tag{18}$$

where w_s is a positive constant, with larger parameter values enhancing the system's interference rejection capability. However, in practical control, excessively high gain can lead to increased system oscillations, typically proportional to w_s.

The overall control, $\mathbf{u}(s)$, can be expressed as:

$$\begin{aligned}\mathbf{u}(s) = \mathbf{u}(s-1) &+ \frac{\rho_1 \hat{\mathbf{\Phi}}_{Lv+1}(s)}{\left\|\hat{\Phi}_{Lv+1}(s)\right\|^2+\sigma}\left(\mathbf{v}_d(s+1) - \mathbf{v}(s) - \hat{\mathbf{J}}(s)\right) \\ &- \frac{\hat{\mathbf{\Phi}}_{Lv+1}(s)}{\left\|\hat{\mathbf{\Phi}}_{Lv+1}(s)\right\|^2+\sigma}\left(\sum_{i=1}^{L_v} \rho_{j+1}\hat{\mathbf{\Phi}}_i^{\mathrm{T}}(s)\Delta\mathbf{v}(s-i+1)\right) \\ &- \frac{\hat{\mathbf{\Phi}}_{Lv+1}(s)}{\left\|\hat{\mathbf{\Phi}}_{Lv+1}(s)\right\|^2+\sigma}\left(\sum_{j=L_v+2}^{L_v+L_u} \rho_j\hat{\mathbf{\Phi}}_j^{\mathrm{T}}(s)\Delta\mathbf{u}(s-L_v-i+1)\right) \\ &- \frac{\hat{\mathbf{\Phi}}_{Lv+1}(s)}{\left\|\hat{\mathbf{\Phi}}_{Lv+1}(s)\right\|^2+\sigma}\left(\frac{\mathbf{e}(s)}{1+hT} - w_s \tanh(\mathbf{\Psi}(s))\right)\end{aligned} \tag{19}$$

The nonlinear system's MFASMC structure using DESO is illustrated for $L_v = 1$ and $L_u = 1$, with the control input and output configuration being similar, in Figure 1.

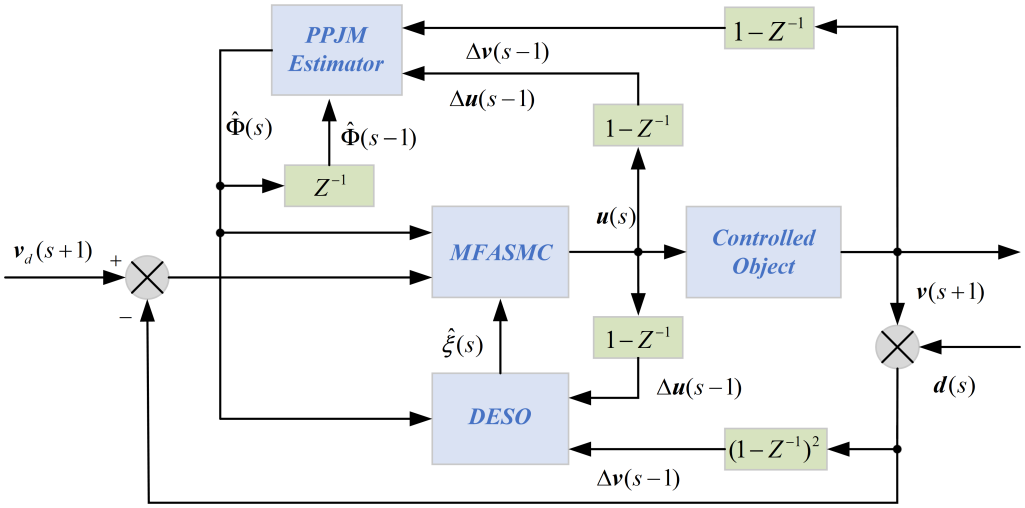

Figure 1. DESO-MFASMC block diagram.

In the figure, MFAC employs real-time updates of pseudo-gradient parameters using nonlinear system I/O data, while DESO utilizes a linearized model to compensate for unknown disturbances during the nonlinear system's operation. This compensation ultimately feeds into the MFASMC controller, which generates control inputs for the nonlinear system, enabling the achievement of the desired objectives.

Remark 2. *The process of this paper is as follows: for discrete general time nonlinear systems, based on the new concept of a pseudo partial derivative, a new equivalent dynamic linearization method for control system design is proposed. Using this method, the discrete-time nonlinear system can be equivalently converted into a dynamic linearization data model based on input/output increment form and FFDL data model. Based on the data model, the designed sliding mode surface and sliding mode function are introduced, and the MFASMC law is obtained. Then, in order to realize real-time compensation of unknown terms in the system, a DESO is obtained based on the dynamic linearized data model and parameter estimation algorithm. For the unknown term of the system, the extended state observer is used to observe and compensate each state of the system and the unknown disturbance, the unknown term is extended to a state variable, and the linear function alignment is used to approximate, which reduces the influence of the integrated unknown term control effect.*

3.3. Convergence Analysis

Using the DESO-MFASMC control algorithm, there is a constant $\lambda_{\min} > 0$, such that when $\lambda > \lambda_{\min}$, there is:

(1) The estimation error of the discrete-time extended observer is bounded.
(2) The estimation error of the unknown PPJM is bounded.
(3) Under the control law, the system ultimately settles into a convergent quasi-sliding mode.
(4) The system output tracking error converges monotonically.

Proof. Firstly, it is proved that the observation error of the DESO is bounded.

Define the state variable $\mathbf{w}(s) = \mathbf{J}(s+1) - \mathbf{J}(s)$, which can be rewritten in the form of Equation (20).

$$\begin{cases} \mathbf{v}(s+1) = \mathbf{v}(s) + \hat{\mathbf{\Phi}}^{\mathrm{T}}(s)\Delta\mathbf{H}(s) + \mathbf{J}(s) \\ \mathbf{J}(s+1) = \mathbf{J}(s) + \mathbf{w}(s) \end{cases} \tag{20}$$

Define $\mathbf{X}(s) = [\mathbf{v}(s), \mathbf{J}(s)]^{\mathrm{T}}$ and $\hat{\mathbf{X}}(s) = [\mathbf{v}_m(s), \hat{\mathbf{J}}(s)]^{\mathrm{T}}$, and then combine Equations (20) and (10) to obtain:

$$\tilde{\mathbf{X}}(s+1) = \mathbf{D}_0\tilde{\mathbf{X}}(s) + \mathbf{D}_1\mathbf{w}(s) \tag{21}$$

where $\tilde{\mathbf{X}}(s) = [\mathbf{v}(s) - \mathbf{v}_m(s), \mathbf{J}(s) - \hat{\mathbf{J}}(s)]^{\mathrm{T}}$, $\mathbf{D}_0 = \begin{bmatrix} \mathbf{W}_1 & \mathbf{I} \\ \mathbf{W}_2 & \mathbf{I} \end{bmatrix}$, and $\mathbf{D}_1 = \begin{bmatrix} 0 \\ \mathbf{I} \end{bmatrix}$; $\mathbf{W}_1 = (1 - l_1)\mathrm{diag}([1, 2, \cdots, n])$; $\mathbf{W}_2 = -l_2\mathrm{diag}([1, 2, \cdots, n])$.

According to the disk theorem, the spectral radius of $\mathbf{D}_0$ is less than 1. By circular disc theorem, there exists a matrix norm such that $\|\mathbf{D}_0\|_v < c_1 < 1$ with $c_1 \in (0, 1)$. Since $\mathbf{J}$ is bounded, $\mathbf{w}$ is also bounded.

Taking the norm of both sides of Equation (21), we obtain:

$$\begin{aligned} \left\|\tilde{\mathbf{X}}(s+1)\right\| &= \left\|\mathbf{D}_0\tilde{\mathbf{X}}(s) + \mathbf{D}_1\mathbf{w}(s)\right\| \le \|\mathbf{D}_0\|\left\|\tilde{\mathbf{X}}(s)\right\| + \|\mathbf{w}(s)\| \\ &\le c_1^{s+1}\left\|\tilde{\mathbf{X}}(0)\right\| + \tfrac{2c_1J_0(1-c_1^s)}{1-c_1} \end{aligned} \tag{22}$$

Thus, the boundedness of the observation error of the DESO can be obtained.

Next, it is shown that the estimation error of PPJM is bounded, denoted by $\tilde{\mathbf{\Phi}}(s) = \hat{\mathbf{\Phi}}(s) - \mathbf{\Phi}(s)$, representing the estimation error of $\mathbf{\Phi}(s)$. Subtracting Equation (6) from $\mathbf{\Phi}(s)$ yields:

$$\begin{aligned} \tilde{\mathbf{\Phi}}(s) &= \hat{\mathbf{\Phi}}(s) - \mathbf{\Phi}(s) + \mathbf{\Phi}(s-1) - \mathbf{\Phi}(s-1) \\ &= \left(\mathbf{I} - \tfrac{\eta\Delta\mathbf{H}(s-1)\Delta\mathbf{H}^T(s-1)}{\mu + \|\Delta\mathbf{H}(s-1)\|^2}\right)\tilde{\mathbf{\Phi}}(s-1) + \mathbf{\Phi}(s-1) - \mathbf{\Phi}(s) \end{aligned} \tag{23}$$

From Assumption 2, it follows that $\|\mathbf{\Phi}(s)\| \le b_0$, which implies $\|\mathbf{\Phi}(s-1) - \mathbf{\Phi}(s)\|$. By taking the norm of both sides of Equation (23) and scaling, we obtain Equation (24).

$$\left\|\tilde{\mathbf{\Phi}}(s)\right\| \le \left\|\left(I - \frac{\eta\Delta\mathbf{H}(s-1)\Delta\mathbf{H}^{\mathrm{T}}(s-1)}{\mu + \|\Delta\mathbf{H}(s-1)\|^2}\right)\tilde{\mathbf{\Phi}}(s-1)\right\| + 2b_0 \tag{24}$$

By squaring the first term of (24), we can obtain:

$$\begin{aligned} &\left\|\left(I - \tfrac{\eta\Delta\mathbf{H}(s-1)\Delta\mathbf{H}^{\mathrm{T}}(s-1)}{\mu + \|\Delta\mathbf{H}(s-1)\|^2}\right)\tilde{\mathbf{\Phi}}(s-1)\right\|^2 \\ &= \left\|\tilde{\mathbf{\Phi}}(s-1)\right\|^2 + \left(-2 + \tfrac{\eta\|\Delta\mathbf{H}(s-1)\|^2}{\mu + \|\Delta\mathbf{H}(s-1)\|^2}\right) \times \tfrac{\eta\left\|\mathbf{H}^{\mathrm{T}}(s-1)\tilde{\mathbf{\Phi}}(s-1)\right\|^2}{\mu + \|\Delta\mathbf{H}(s-1)\|^2} \end{aligned} \tag{25}$$

where $0 < \eta < 2$ and $\mu > 0$, which implies $-2 + \eta\|\Delta\mathbf{H}(s-1)\|^2/(\mu + \|\Delta\ \mathbf{H}(s-1)\|^2) < 0$. Then, we can obtain:

$$\left\| \left(I - \frac{\eta \Delta\mathbf{H}(s-1)\Delta\mathbf{H}^{\mathrm{T}}(s-1)}{\mu + \|\Delta\mathbf{H}(s-1)\|^2} \right) \tilde{\mathbf{\Phi}}(s-1) \right\|^2 < \left\| \tilde{\mathbf{\Phi}}(s-1) \right\|^2 \tag{26}$$

There must be a constant $0 < d_1 < 1$ such that (27) holds.

$$\left\| \tilde{\mathbf{\Phi}}(s-1) - \frac{\eta \tilde{\mathbf{\Phi}}(s-1)\Delta\mathbf{H}(s-1)\Delta\mathbf{H}^{\mathrm{T}}(s-1)}{\mu + \|\Delta\mathbf{H}(s-1)\|^2} \right\| \leq d_1 \left\| \tilde{\mathbf{\Phi}}(s-1) \right\| \tag{27}$$

Substituting Equation (27) into Equation (24), we obtain Equation (28).

$$\begin{array}{c} \left\| \tilde{\mathbf{\Phi}}(s) \right\| \leq d_1 \left\| \tilde{\mathbf{\Phi}}(s-1) \right\| + 2b_0 \leq d_1^2 \left\| \tilde{\mathbf{\Phi}}(s-2) \right\| + 2(1+d_1)b_0 \\ \leq \cdots \leq d_1^s \left\| \tilde{\mathbf{\Phi}}(0) \right\| + \frac{2b_0(1-d_1^s)}{(1-d_1)} \end{array} \tag{28}$$

From Equation (28), it follows that $\tilde{\mathbf{\Phi}}(s)$ is bounded, and from the Assumption 2, $\mathbf{\Phi}(s)$ is bounded, that is, $\|\mathbf{\Phi}(s)\| \leq b_0$, then $\left\|\hat{\mathbf{\Phi}}(s)\right\|$ is bounded.

Substituting Equations (10) and (19) into Equation (16), we have:

$$\Delta\Psi_i(s+1) = -(1+hT)w_s \tanh(\Psi_i(s)) + \Delta J_i \tag{29}$$

When $\Psi_i(s) > 0$:

$$\Psi_i(s+1) - \Psi_i(s) = -(1+hT)w_s + \Delta J_i < 0 \tag{30}$$

When $\Psi_i(s) < 0$:

$$\Psi_i(s+1) - \Psi_i(s) = (1+hT)w_s + \Delta J_i > 0 \tag{31}$$

Combining Equations (30) and (31) yields:

$$|\Psi_i(s+1) - \Psi_i(s)| = (1+hT)w_s + \Delta J_i \tag{32}$$

$$|\Psi_i(s+1)| < |\Psi_i(s)| s > s_0 \tag{33}$$

$$\begin{cases} [\Psi_i(s+1) - \Psi_i(s)]\mathrm{sgn}(\Psi_i(s)) < 0 \\ [\Psi_i(s+1) + \Psi_i(s)]\mathrm{sgn}(\Psi_i(s)) > 0 \end{cases} \tag{34}$$

Equation (33) is equivalent to Equation (34). Consequently, if Equation (34) holds, this implies that $\Psi_i(s)$ is monotonically decreasing and converges to the sliding surface in finite time s_0.

Next, it is proved that the tracking error of the controller is bounded and converges to a constant value.

By substituting Equation (4) in Equation (19), we have:

$$\begin{array}{l} \mathbf{e}(s+1) = \mathbf{v}_d(s+1) - \mathbf{v}(s+1) \\ = \mathbf{v}_d(s+1) - \mathbf{v}(s) - \hat{\mathbf{\Phi}}^{\mathrm{T}}(s)\Delta\mathbf{H}(s) - \mathbf{J}(s) \\ = \mathbf{v}_d(s+1) - \mathbf{v}(s) - \rho_1\hat{\mathbf{\Phi}}_1(s)\Delta\mathbf{v}(s) - \cdots \\ - \rho_{L_v}\hat{\mathbf{\Phi}}_{L_v}(s)\Delta\mathbf{v}(s-L_v) - \rho_{L_v+1}\hat{\mathbf{\Phi}}_{L_v+1}(s)\Delta\mathbf{u}(s) - \cdots \\ - \rho_{L_v+L_u}\hat{\mathbf{\Phi}}_{L_v+L_u}(s)\Delta\mathbf{u}(s-L_u) - \hat{\mathbf{J}}(s) \\ = \frac{1}{1+hT}\mathbf{e}(s) - w_s \cdot \tanh(\mathbf{\Psi}(s)) - \hat{\mathbf{J}}(s) \end{array} \tag{35}$$

Further Equation (35) is written as:

$$e_i(s) = \frac{1}{1+hT}e_i(s) - w_s \cdot \tanh(\Psi_i(s)) - \hat{J}_i(s) \tag{36}$$

It can be deduced that $w_s \tanh(\Psi_i(s)) \in [-w_s, w_s]$ is a bounded constant. Let κ be another constant, with $\kappa \geq |w_s|$. Then, there exists a positive scalar b_4 such that:

$$0 < \frac{1}{1+hT} < b_4 < 1 \tag{37}$$

Thus,

$$\begin{aligned} e_i(s+1) &\leq b_4 e_i(s) + \kappa + J_0 \leq b_4^2 e_i(s-1) + (1+b_4)(\kappa + J_0) \\ &\leq \cdots \leq b_4^s e_i(1) + \tfrac{1-b_4^s}{1-b_4}(\kappa + J_0) \end{aligned} \tag{38}$$

Equation (38) demonstrates the bounded convergence of the tracking error. Proof completed. □

4. Optimization and Tuning of Controller Parameters Based on GA

Controller design is the most important part of the controlled system operation process, and its parameter selection is a direct factor affecting the effect of the same controller control. The parameters of the MFASMC are numerous, including ρ, σ, μ, η, etc. To avoid the subjectivity of manual system debugging and reduce the time cost of manually adjusting parameters, this paper introduces a neural network algorithm for controller parameter optimization and tuning. The cumulative mean square error of system output error is selected as the loss function as shown in Equation (39).

$$fit(x) = \sum_{s=1}^{S} [\mathbf{v}(s) - \mathbf{v}_d(s)]^{\mathrm{T}} [\mathbf{v}(s) - \mathbf{v}_d(s)] \tag{39}$$

where x is the setting parameter, $x = [\eta, \mu, \rho, \sigma, b_2, \alpha, b_1, h, w_s, l_1, l_2, \Phi(1)]^{\mathrm{T}}$. The requirements of each parameter are $0 < \eta \leq 2$, $\mu > 0$, $0 < \rho \leq 1$, $\sigma > 0$, $\alpha > 1$, $b_2 > b_1(2\alpha + 1)(n-1)$, $h > 0$, $w_s > 0$, $l_1 > 0$, $l_2 > 0$, $\left|\Phi_{(L_u+1)ij}(1)\right| \leq b_1$, $b_2 \leq \left|\Phi_{(L_u+1)ii}(1)\right| \leq \alpha b_2$.

To meet the parameter requirements, adding a penalty factor transforms the parameter-tuning problem of the model-free adaptive sliding mode controller into the unconstrained optimization problem shown in Equation (40).

$$\begin{aligned} \min fit(x) = \sum_{s=1}^{S} [\mathbf{v}(s) - \mathbf{v}_d(s)]^{\mathrm{T}} [\mathbf{v}(s) - \mathbf{v}_d(s)] + K_1 \begin{pmatrix} g(\mu + \sigma + b_1 + h + w_s + l_1 + l_2) + g(2-\eta) \\ + g(1-\rho) \end{pmatrix} \\ + K_2 \begin{pmatrix} g(b_1 - \Phi_{(L_v+1)ij}(1)) + g(\Phi_{(L_v+1)ii}(1) - b_2) \\ g(\alpha b_2 - \Phi_{(L_v+1)ii}(1)) \end{pmatrix} \end{aligned} \tag{40}$$

where K_1 and K_2 are penalty factors and $g(x) = \begin{cases} 1, x \leq 0 \\ 0, x > 0 \end{cases}$.

With the fitness function given by Equation (40), the parameters of the DESO-MFASMC are tuned.

As shown in Figure 2, firstly, the objective function is determined as Equation (40), and the population is initialized. The initial parameters are selected and input into the fitness function to calculate the corresponding fitness values, and then if the stop condition is met is checked. Elite individuals are replicated, while the remaining individuals undergo crossover and, finally, mutate to obtain new parameter values. The calculation is carried out and if the conditions are met is determined. The evolution process is repeated until the desired parameter values are obtained.

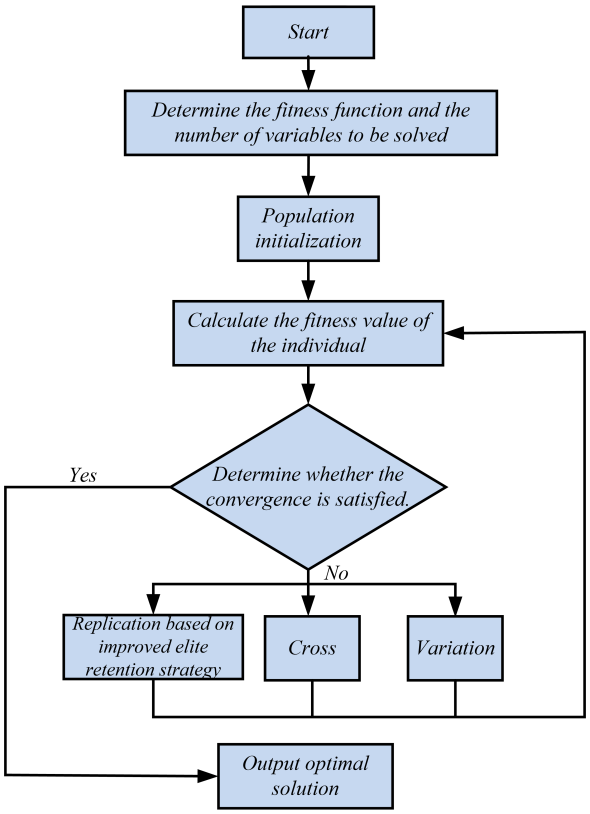

Figure 2. Genetic algorithm flowchart.

5. Simulation and Experiment

This section consists of two sections: numerical simulation and semi-physical simulation. Firstly, through typical MIMO numerical experiments, the effectiveness of the proposed algorithm (DESO-MFASMC) is compared with MFAC. The next set of experiments incorporates external disturbances and implements the approach proposed in this study for controlling electric heavy-duty forklifts, while also comparing MFAC with traditional PID control. Additionally, the experiments explore the robustness and adaptability of the algorithm in practical applications, further demonstrating its potential in engineering contexts.

5.1. Experiment 1: Numerical Simulation

To enhance the applicability of the proposed method, we extended DESO-MFASMC to a MIMO system and verified its effectiveness by simulating a typical controlled object. We compared and simulated the DESO-MFASMC and FFDL-MFAC algorithms using time-varying signals. The first group of simulation objects consisted of a system with three inputs and three outputs, as follows:

$$\begin{cases} v_1(s+1) = 1.5 \times v_1(s) + 0.12 \times {v_1}^2(s-1) + 0.7 \times u_1(s) \\ \qquad +0.3 \times u_2(s) + 0.3 \times u_3(s) + d_1(s) \\ v_2(s+1) = 1.6 \times v_2(s) + 0.14 \times v_2^2(s-1) + 0.4 \times u_1(s) \\ \qquad +0.6 \times u_2(s) + 0.3 \times u_3(s) + d_2(s) \\ v_3(s+1) = 1.6 \times v_3(s) + 0.15 \times v_3^2(s-1) + 0.1 \times u_1(s) \\ \qquad +0.7 \times u_2(s) + 0.6 \times u_3(s) + d_3(s) \end{cases} \tag{41}$$

where $d_i(s)$ represents a zero-mean, zero-variance noise signal with a standard deviation of 0.025.

The sampling period is set to 1 s and the number of sampling samples is 1000. When comparing various control methods, the same data are used for the controller design. A genetic algorithm is used for parameter tuning, with a maximum genetic

generation of 500, a population size of 100, a mutation probability of 0.2, a crossover probability of 0.7, and penalty factors all set to 100. The genetic algorithm achieves the target function requirement after 238 evolutions. The controller parameters are set as: $\eta = 0.1202$, $\mu = 0.6668$, $\rho_1 = 0.9691$, $\rho_2 = 0.9919$, $\sigma = 6.0335 \times 10^{-6}$, $b_2 = 0.037$, $\alpha = 19.7351$, $b_1 = 0.0029$, $h = 0.2637$, $w_s = 0.5635$, $l_1 = 0.2297$, $l_2 = 5.4816 \times 10^{-5}$, and $\hat{\mathbf{\Phi}}(1) = \hat{\mathbf{\Phi}}(2) = \text{diag}\{0.55, 0.6, 0.55\}$.

Figure 3 displays the output curve of the MIMO system (41) under the DESO-MFASMC and MFAC methods, while Figure 4 shows the error curves of these two methods. Zooming in on the details in Figure 3, it is evident that at the 100th and 200th seconds, due to phase delay and poor anti-interference ability, MFAC fails to timely feedback the output signal, resulting in significant tracking delays and oscillations, thereby weakening its fast response characteristics. In contrast, the enhanced DESO-MFASMC method promptly provides feedback on the output signal, effectively eliminating interference while maintaining the fast response characteristics of the MFAC algorithm. By the 200th second, even with changes in the reference signal, DESO-MFASMC maintains a stable convergence state, demonstrating the further adaptability of the algorithm. Table 1 lists the corresponding performance metrics of these two methods. It is noteworthy that when employing the DESO-MFASMC method, the MAE and MSE are approximately twice and six times higher, respectively, than those of the MFAC method. Particularly with complex reference signals, DESO-MFASMC exhibits significantly improved tracking performance. The proposed algorithm adopts a model-free design, utilizing FFDL data models to design a DESO, selecting an integral sliding mode surface to eliminate chattering during the switching phase, and achieving smooth transitions through the use of a hyperbolic tangent function with small slope changes. Furthermore, the DESO method effectively estimates uncertainties in discrete systems, thereby enhancing system robustness and tracking control performance.

Figure 5 illustrates the control input diagrams for each control scheme. Throughout all stages, the inputs of the DESO-MFASMC scheme change smoothly. During predetermined signal changes, the inputs also adjust at a low rate, reducing system oscillations. Conversely, the MFAC scheme shows significant input changes, leading to more severe system oscillations.

(1) MAE

$$\text{MAE} = \frac{1}{nS} \sum_{i=1}^{n} \sum_{s=1}^{S} |v_i(s) - v_d(s)| \tag{42}$$

(2) MSE

$$\text{MSE} = \frac{1}{nS} \sum_{i=1}^{n} \sum_{s=1}^{S} |v_i(s) - v_d(s)|^2 \tag{43}$$

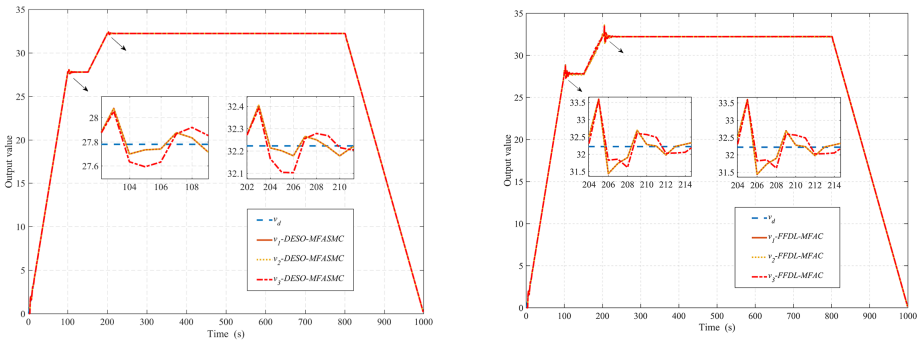

(**a**) (**b**)

Figure 3. Output curves. (**a**) DESO-MFASMC; (**b**) MFAC.

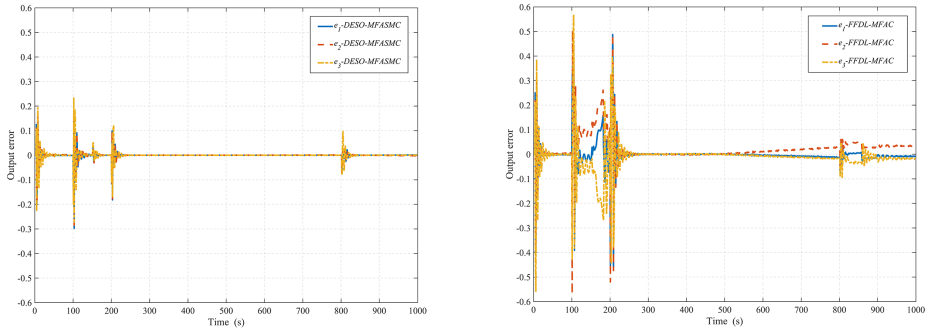

(**a**) (**b**)

Figure 4. Error curves. (**a**) DESO-MFASMC; (**b**) MFAC.

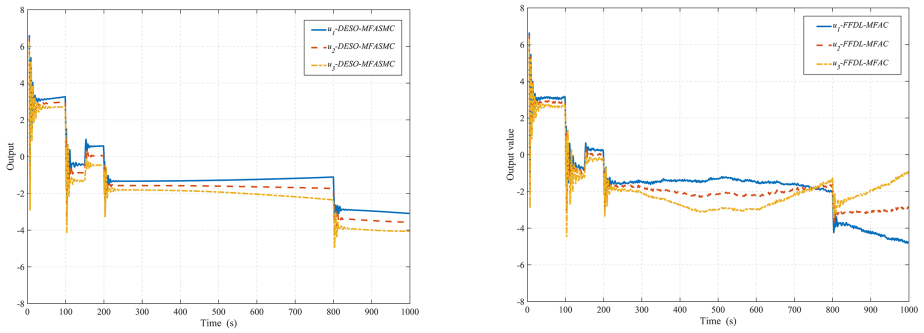

(**a**) (**b**)

Figure 5. Input curves. (**a**) DESO-MFASMC; (**b**) MFAC.

In conclusion, this paper adopts integral sliding mode function based on MFASMC to reduce the chattering issue generated by conventional sliding modes, enhance the stability of the controller, and improve the control accuracy. Furthermore, this paper introduces a discrete extended state observer in the controller design for real-time compensation to alleviate the impact of external disturbances on the control effectiveness.

Table 1. Performance indexes.

METHODS	MFAC	DESO-MFASMC
Rise time (s)	5	3
Adjust time (s)	22	8
MAE	1.48×10^{-2}	6.27×10^{-3}
MSE	1.52×10^{-2}	2.45×10^{-3}

5.2. Experiment 2: Electric Forklift

Electric transport forklifts are key equipment in modern logistics and manufacturing industries, designed for the efficient handling and transportation of heavy goods. These forklifts typically use an electric drive system, which has significant environmental advantages over traditional internal combustion engine forklifts, such as zero emissions and low noise. Their core components include a sturdy chassis and drive system, consisting of an electric motor, transmission device, and reinforced wheels, ensuring reliable operation in different terrains and work environments [38,39]. The control system is designed to be simple and intuitive, allowing operators to control the lifting and tilting of the forks through levers and a dashboard for precise cargo handling, as shown in Figure 6. Electric transport forklifts are also equipped with advanced batteries and charging systems to support long hours of continuous work, meeting the demands of efficient operations. The drive system of an electric forklift is crucial, comprising traction motors, control systems (such as motor drives, controllers, and various sensors), mechanical reduction and transmission devices,

and wheels. Their operational performance largely depends on advanced drive system speed control technology, currently utilizing two main drive speed control systems: direct current and alternating current. Overall, electric transport forklifts have become indispensable tools in modern logistics and manufacturing industries by improving handling efficiency, reducing operating costs, and minimizing environmental impact.

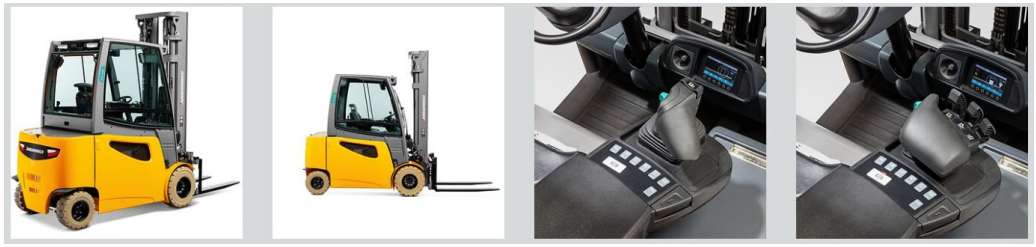

Figure 6. Electric forklift operation.

Regarding the electric forklift as a particle, the force analysis is shown in Figure 7. The main forces include the driving force and braking force provided by the electric drive system, which is used to change its speed and stop the movement; the gravity generated by the load of the forklift affects its stability and driving ability; and air resistance and rolling resistance. In summary, the dynamic equation of the forklift running state can be obtained as follows [32,33].

$$ma_{\mathrm{h}} = \frac{F_{\mathrm{t}} - F_{\mathrm{f}} - F_{\mathrm{w}} - F_{\mathrm{b}} - F_{g}}{\delta} \tag{44}$$

where $F_{\mathrm{t}} = \frac{T_{\mathrm{e}} i_{\mathrm{g}} i_0 \eta_{\mathrm{T}}}{r}$; $F_{\mathrm{f}} = mgf\cos F$; $F_{\mathrm{w}} = \frac{1}{2} C_{\mathrm{D}} A \rho u_{\mathrm{r}}^2$; $F_{\mathrm{b}} = k_{\mathrm{b}} p_{\mathrm{b}}$; $F_{\mathrm{g}} = mg\sin F$. F_{t} is driving force; F_{f} is rolling resistance; F_{w} is air resistance; F_{b} is wheel braking force; T_{e} is motor torque; i_{g} is motor transForce analysis of electric balanced forklift mission ratio; i_0 is transmission ratio of reducer; η_{T} is transmission efficiency; f is rolling resistance coefficient; C_{D} is air resistance coefficient; a is windward area; and ρ is air density. From Equation (44), the desired motor torque T_{des} can be obtained by the expected acceleration a_{des}:

$$T_{\mathrm{des}} = \frac{\left(mgf\cos F + mg\sin F + \frac{1}{2} C_{\mathrm{D}} A \rho u_{\mathrm{r}}^2 + k_{\mathrm{b}} p_{\mathrm{b}} + \delta m a_{\mathrm{h}}\right) r}{i_{\mathrm{g}} i_0 \eta_{\mathrm{T}}} \tag{45}$$

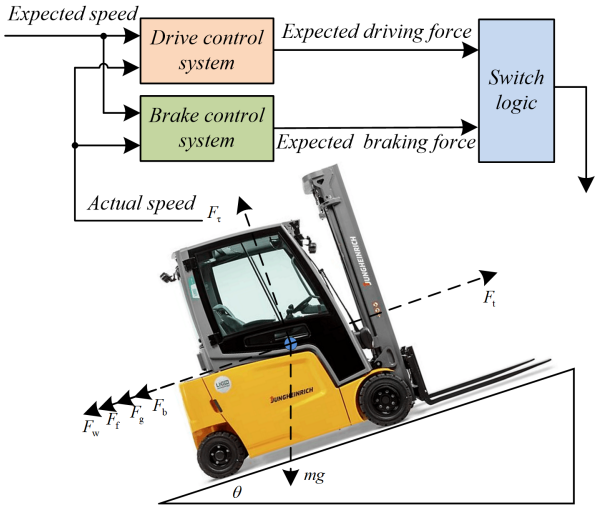

Figure 7. Force analysis.

For the braking conditions, the relationship between p_b and F_b applied to the wheels can be regarded as linear. Therefore, under the braking condition, we can obtain the desired braking force p_{des} as

$$p_{des} = \left(\frac{\delta m a_h + \frac{T_e i_g i_0 \eta_T}{r} + mgf\cos F + mg\sin F + \frac{1}{2} C_D A \rho u_r^2}{k_b} \right) \tag{46}$$

This paper collects real-time control force and speed data from electric forklifts and employs recursive least squares online identification to estimate the parameters of the longitudinal dynamic model in real-time, with continuous updates.

Based on (44)–(46), the dynamic equations describing the relationship between control force and speed for the electric forklift are

$$E(z^{-1})v(s) = G(z^{-1})u(s-1) + \frac{P(z^{-1})\Upsilon(s)}{1-z^{-1}} \tag{47}$$

The corresponding system parameters are

$$\begin{cases} E(z^{-1}) = 1 + E_0 z^{-1} + \cdots + E_{n_E} z^{-n_E} \\ G(z^{-1}) = G_0 + G_1 z^{-1} + \cdots + G_{n_G} z^{-n_G} \\ P(z^{-1}) = 1 + P_1 z^{-1} + \cdots + P_{n_P} z^{-n_P} \end{cases} \tag{48}$$

Rewrite (48) to the following form

$$\begin{aligned} \Delta v(s) &= [1 - E(z^{-1})]\Delta v(s) + G(z^{-1})\Delta u(s-1) + \Upsilon(s) \\ &= \mathbf{Q}^{\mathrm{T}}(s)\mathbf{F} + \Upsilon(s) \end{aligned} \tag{49}$$

where $\mathbf{Q}(s)$ and $\mathbf{F}(s)$ are data vectors and model parameters, respectively, defined as

$$\begin{cases} \mathbf{Q}(s) = [-\Delta v(s-1), \cdots, -\Delta v(s-n_a), \Delta u(s-1), \cdots, \Delta u(s-n_b-1)]^{\mathrm{T}} \\ \mathbf{F} = [E_1, \cdots, E_{n_E}, G_0, \cdots, G_{n_G}]^{\mathrm{T}} \end{cases} \tag{50}$$

The unknown parameter vector is estimated using the recursive least squares algorithm with forgetting factor, as described in [33].

$$\begin{cases} \hat{\mathbf{F}}(s) = \hat{\mathbf{F}}(s-1) + \mathbf{M}(s)[\Delta v(s) - \mathbf{Q}^{\mathrm{T}}(s)\hat{\mathbf{F}}(s-1)] \\ \mathbf{M}(s) = \frac{\mathbf{C}(s-1)\mathbf{Q}(s-1)}{\lambda + \mathbf{Q}^{\mathrm{T}}(s)\mathbf{C}(s-1)\mathbf{Q}(s)} \\ \mathbf{C}(s) = \frac{1}{\lambda}\left[\mathbf{I} - \mathbf{M}(s)\mathbf{Q}^{\mathrm{T}}(s)\right]\mathbf{C}(s-1) \end{cases} \tag{51}$$

where λ is the forgetting factor, with values ranging from 0.9 to 1.

To validate the effectiveness of DESO-MFASMC, this section conducts a simulation experiment on an electric forklift as the controlled object, recording control forces, speed, and other data. The control block diagram is depicted in Figure 8, and the forklift parameters are listed in Table 2. Simulations with DESO-MFASMC, MFAC, and PID are performed for comparison, analyzing tracking errors, changes in driving force, and acceleration. The superiority of the DESO-MFASMC method is demonstrated through these analyses. For the DESO-MFASMC and MFAC method: $\eta = 0.15$, $\mu = 0.7$, $\rho_1 = 0.9$, $\rho_2 = 1$, $\sigma = 6 \times 10^{-5}$, $b_2 = 0.07$, $\alpha = 0.2$, $b_1 = 0.03$, $h = 0.247$, $w_s = 0.56$, $l_1 = 0.3$, $l_2 = 1.5 \times 10^{-5}$, and $\hat{\Phi}(1) = \hat{\Phi}(2) = [0.3, 0.3]$. For the PID method: $v(1) = v_d(1)$, $K_p = 0.65$, $K_i = 0.7$, and $K_d = 0.06$.

Table 2. EFG-BC/320 forklift and control parameters.

Parameter Name	-	Parameter Name	-
Forklift model	EFG-BC/320	Control method	DESO-MFASMC
Maximum speed	18 km/h	Load capacity	2000 kg
Overall length	3096 mm	Power system	Electric drive (48 V)
System parameter	i_g=3.95, C_D=0.75, k_b=1.23, A=1.85 $f = 0.05, m = 3820$kg	-	-
Input and output data	Speed, position and driving force sensors	Control accuracy	±0.132 m/s (velocity tracking error)

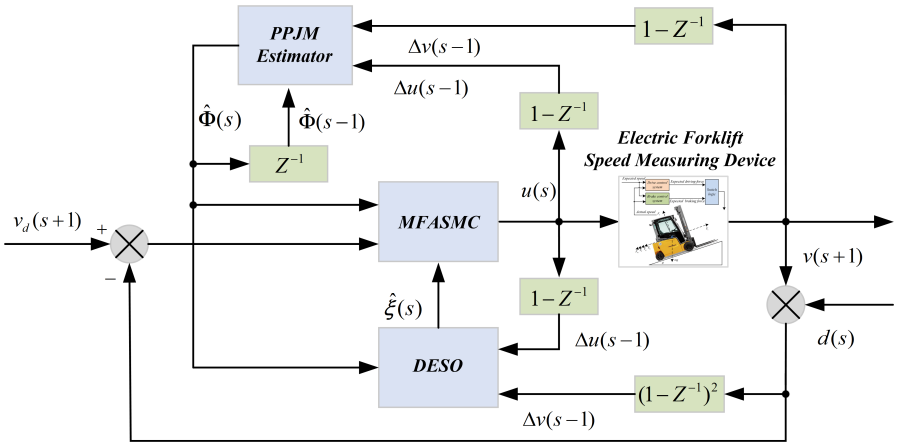

Figure 8. DESO-MFASMC for Electric forklift.

Figures 9 and 10 display the speed and error curves for the electric heavy-duty forklift using DESO-MFASMC, MFAC, and PID. MFAC and PID errors fluctuate between [−0.052 m/s, 0.068 m/s] and [−0.738 m/s, 0.136 m/s], respectively. In contrast, DESO-MFASMC employs full-state MFAC, with parameters optimized by a genetic algorithm and an extended state observer for system disturbances and uncertainties, significantly enhancing robustness and convergence. This achieves a speed error range of [−0.031 m/s, 0.048 m/s] during operation, with low sensitivity to disturbances. DESO-MFASMC shows superior tracking accuracy and robustness compared to MFAC and PID. Simulations confirm DESO-MFASMC's ability to effectively suppress measurement disturbances from sensor noise and external interference, thus improving the operational safety and reliability of the forklift. The proposed algorithm's performance in complex conditions demonstrates strong potential for practical applications.

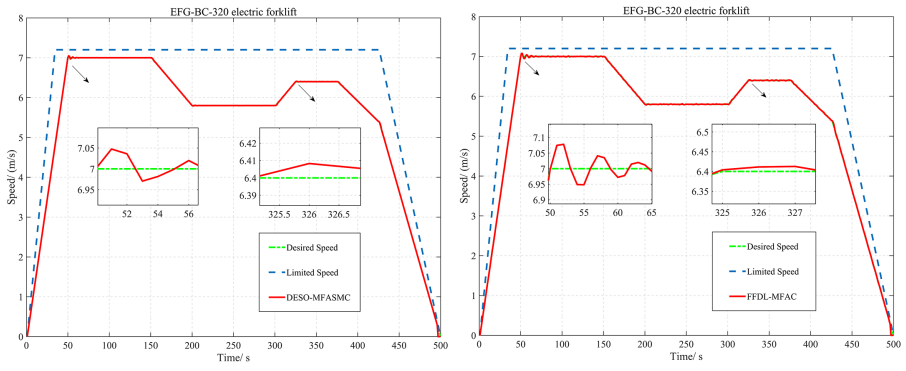

(**a**) (**b**)

Figure 9. *Cont.*

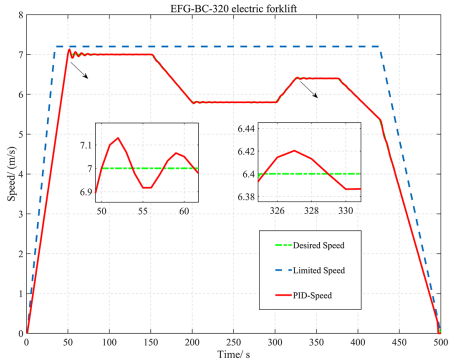

(**c**)

Figure 9. Output curves. (**a**) DESO-MFASMC; (**b**) MFAC; (**c**) PID.

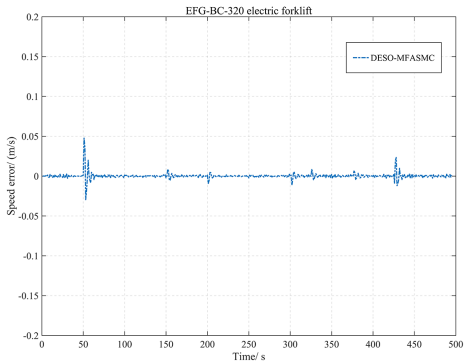

(**a**)

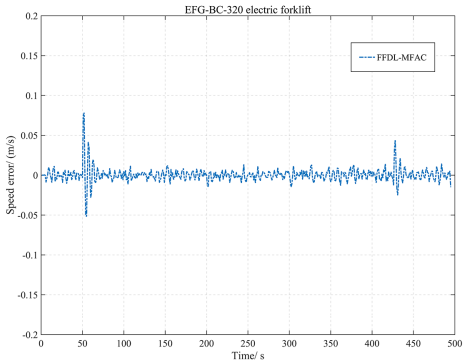

(**b**)

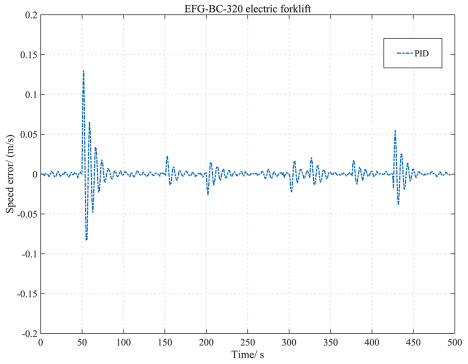

(**c**)

Figure 10. Output error curves. (**a**) DESO-MFASMC; (**b**) MFAC; (**c**) PID.

Figure 11 illustrates the curves of driving force and braking force for electric forklifts when controlled by DESO-MFASMC, MFAC, and PID. As can be observed from Figure 11, the force ranges for driving and braking under MFAC and PID methods are [−610 N, 423 N] and [−412 N, 634 N], respectively, which exhibit significant fluctuations, frequent changes in operating conditions, and large system oscillations. In contrast, the control force variation with DESO-MFASMC is more stable, with minimal system overshoot, effectively mitigating changes during the transition phase. The force range for driving and braking using DESO-MFASMC is [−408 N, 405 N].

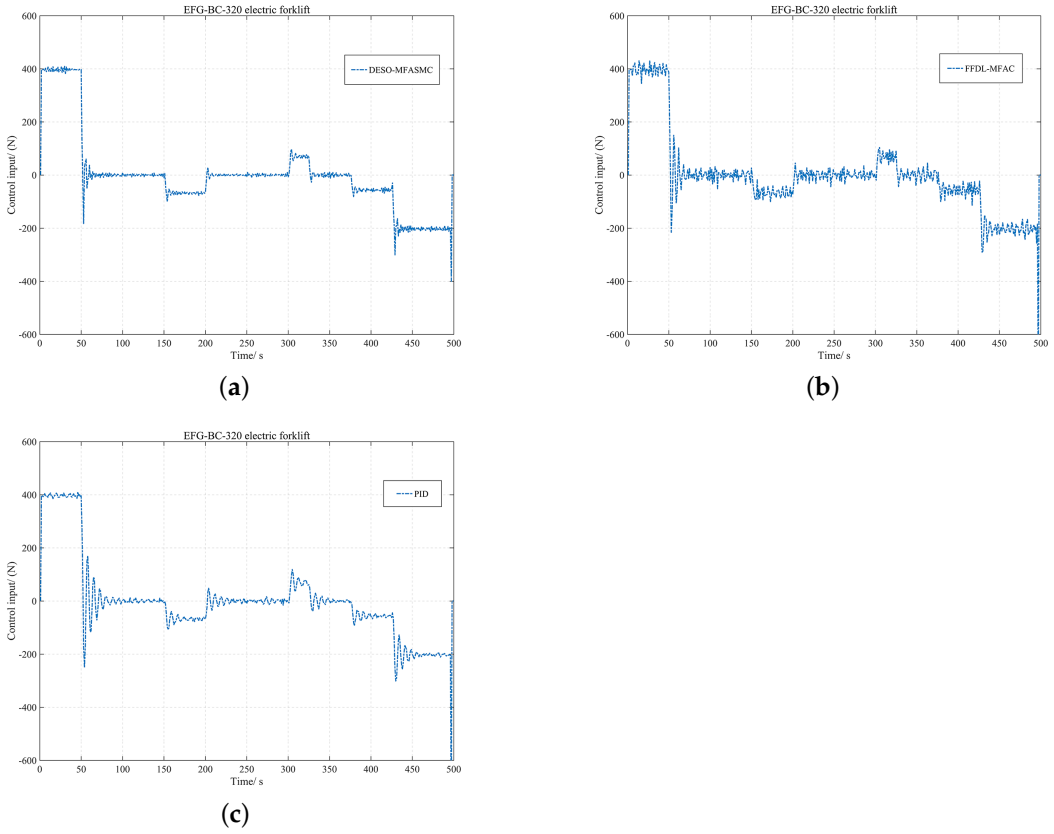

Figure 11. Input curves. (**a**) DESO-MFASMC; (**b**) MFAC; (**c**) PID.

Figure 12 shows the acceleration change curve of the electric heavy-duty forklift under the action of DESO-MFASMC, MFAC, and PID. It can be seen from the figure that the acceleration ranges of MFAC and PID are $[-0.192\ \mathrm{m{\cdot}s^{-2}}, 0.114\ \mathrm{m{\cdot}s^{-2}}]$ and $[-0.216\ \mathrm{m{\cdot}s^{-2}}, 0.108\ \mathrm{m{\cdot}s^{-2}}]$, respectively. In contrast, under the action of DESO-MFASMC, the acceleration change of the electric forklift is gentle, with a range of $[-0.105\ \mathrm{m{\cdot}s^{-2}}, 0.104\ \mathrm{m{\cdot}s^{-2}}]$, ensuring the safe operation of the electric forklift and preventing overturning during the handling process. Furthermore, the performance metrics (52) and (53) are used to evaluate the DESO-MFASMC, MFAC, and PID schemes, as shown in Table 3. In Table 3, the MSE and IAE values of MFAC and PID are both greater than those of DESO-MFASMC.

(1) MAE

$$\mathrm{MAE} = \frac{1}{S}\sum_{s=1}^{S}|v(s) - v_d(s)| \tag{52}$$

(2) MSE

$$\mathrm{MSE} = \frac{1}{S}\sum_{s=1}^{S}|v(s) - v_d(s)|^2 \tag{53}$$

Table 3. Performance indexes.

Methods	PID	MFAC	DESO-MFASMC
Adjust time (s)	26	17	6
MAE	6.21×10^{-2}	4.38×10^{-2}	1.84×10^{-2}
MSE	3.14×10^{-3}	7.41×10^{-4}	2.08×10^{-4}

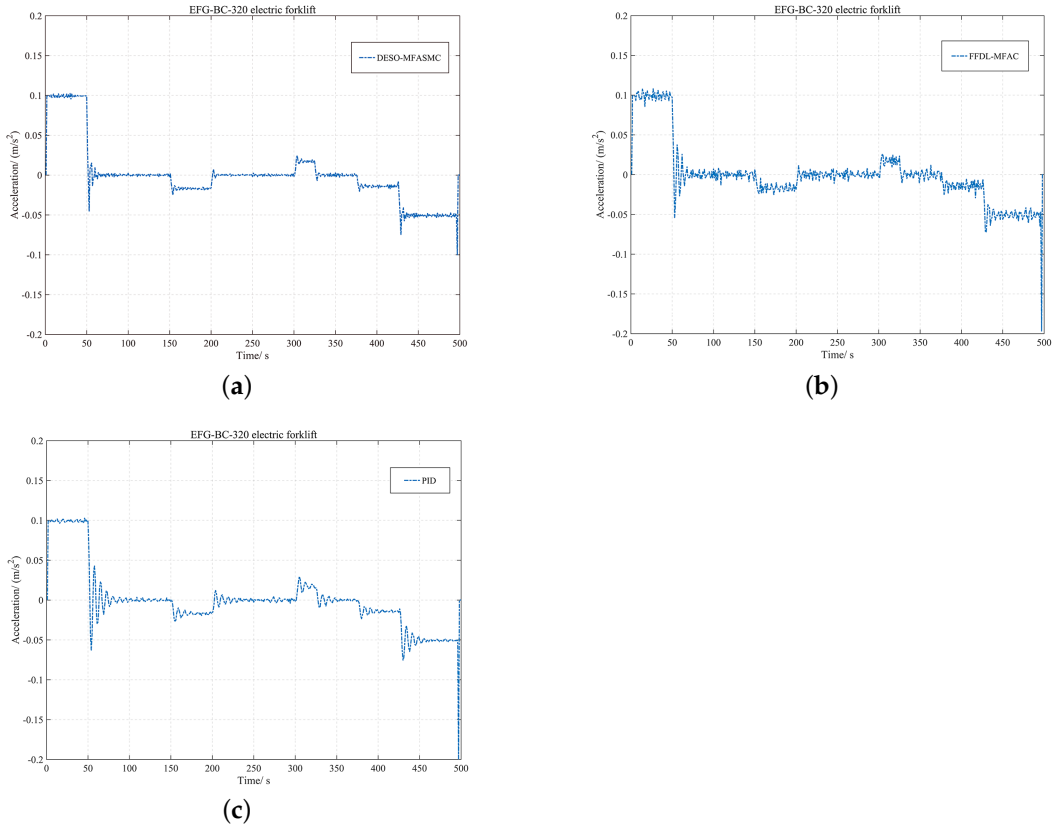

Figure 12. Acceleration curves. (**a**) DESO-MFASMC; (**b**) MFAC; (**c**) PID.

6. Conclusions

To handle the problem of low accuracy in trajectory tracking control of general nonlinear discrete-time systems, a novel MFASMC algorithm based on a DESO is proposed. This algorithm combines full-format MFAC and active disturbance rejection, and the parameters are tuned using a genetic algorithm. After determining the coefficients, simulation experiments were conducted to evaluate the algorithm's performance. The results indicate that the DESO-MFASMC algorithm not only enhances the tracking accuracy of nonlinear systems but also reduces dependence on models in DSMC. The introduction of the extended state observer helps to observe uncertainties and disturbances, and promptly compensates the controller, increasing its practical utility.

Future work will include the following: The effects of different transport types and delays will be considered and external disturbances taken into account; some intelligent algorithms will be introduced to further optimize DESO-MFASMC control parameters. The problem of coordination and formation control in multi-agent systems is a hot topic in the control field. Therefore, a multi-agent coordination and formation control scheme should be studied in the future. The control performance of DESO-MFASMC is further improved by improving the sliding mode surface and sliding mode reaching rate. Future research directions also include optimizing the computational efficiency and performance of the algorithms, exploring their applicability in complex systems and wider application scenarios, and improving their learning capabilities through deep learning and reinforcement learning techniques. Further experimental verification and refinement of parameter optimization strategies will better meet the increasingly complex and diverse engineering control needs. It is important to note that it is important to adjust controller parameters adaptively without using model information. For example, the parameter tuning methods of PID control include iterative feedback tuning, virtual reference feedback tuning, etc., which are all data-driven methods. Therefore, in our research in the near future, we will develop the tuning mechanism of controller parameters by referring to these methods to im-

prove the control performance. In addition, the uncertainties such as random [40], frictional effect [41], input saturation, and output constraint are not considered in the design and analysis of the controller in this work, making them important topics for future research.

Author Contributions: Conceptualization, X.W. and Z.S.; validation, Z.S. and J.X.; formal analysis, F.X.; data curation, Y.W.; writing—original draft, X.W.; writing—review and editing, Z.S. and H.P.; supervision, X.W. and Z.S. All authors have read and agreed to the published version of the manuscript.

Funding: This research was funded by the Quzhou City Science and Technology Plan projects: (2023K263, 2023K265, 2023K045) and General Research Projects of the Zhejiang Provincial Department of Education (2023): (Y202353440, Y202353289).

Data Availability Statement: No new data were created or analyzed in this study.

Conflicts of Interest: Hanzhou Peng was employed by the company China Railway Guangzhou 380 Group Co., Ltd. Changsha Electric Service Depot. Yulong Wang was employed by the company Quzhou Special Equipment Inspection & Testing Research Institute. The remaining authors declare that the research 381 was conducted in the absence of any commercial or financial relationships that could be construed as 382 a potential conflict of interest.

Appendix A

For the convenience of the readers, the proof is rewritten here. From MIMO system (1)

$$\begin{aligned}\Delta\mathbf{v}(s+1) =&\mathbf{f}(\mathbf{v}(s),\ \cdots,\ \mathbf{v}(s-p_v),\mathbf{u}(s),\ \cdots,\ \mathbf{u}(s-p_u))\\ &-\mathbf{f}(\mathbf{v}(s-1),\ \cdots,\ \mathbf{v}(s-p_v-1),\mathbf{u}(s-1),\ \cdots,\ \mathbf{u}(s-p_u-1))\end{aligned} \tag{A1}$$

Using Assumption 1 and the Cauchy's mean value theorem on (54) gives

$$\begin{aligned}\Delta\mathbf{v}(s+1) =& \frac{\partial\mathbf{f}^*}{\partial\mathbf{v}(s)}\Delta\mathbf{v}(s)+\ldots+\frac{\partial\mathbf{f}^*}{\partial\mathbf{v}(s-p_v)}\Delta\mathbf{v}(s-p_v)\\ &+\frac{\partial\mathbf{f}^*}{\partial\mathbf{u}(s)}\Delta\mathbf{u}(s)+\ldots+\frac{\partial\mathbf{f}^*}{\partial\mathbf{u}(s-p_u)}\Delta\mathbf{u}(s-p_u)\end{aligned} \tag{A2}$$

where

$$\begin{aligned}\frac{\partial\mathbf{f}^*}{\partial\mathbf{v}(s-i)} &= \begin{bmatrix}\frac{\partial f_1^*}{\partial v_1(s-i)} & \frac{\partial f_1^*}{\partial v_2(s-i)} & \cdots & \frac{\partial f_1^*}{\partial v_n(s-i)}\\ \frac{\partial f_2^*}{\partial v_1(s-i)} & \frac{\partial f_2^*}{\partial v_2(s-i)} & \cdots & \frac{\partial f_2^*}{\partial v_n(s-i)}\\ \vdots & \vdots & \ddots & \vdots\\ \frac{\partial f_n^*}{\partial v_1(s-i)} & \frac{\partial f_n^*}{\partial v_2(s-i)} & \cdots & \frac{\partial f_n^*}{\partial v_n(s-i)}\end{bmatrix}\\ \frac{\partial\mathbf{f}^*}{\partial\mathbf{u}(s-j)} &= \begin{bmatrix}\frac{\partial f_1^*}{\partial u_1(s-j)} & \frac{\partial f_1^*}{\partial u_2(s-j)} & \cdots & \frac{\partial f_1^*}{\partial u_n(s-j)}\\ \frac{\partial f_2^*}{\partial u_1(s-j)} & \frac{\partial f_2^*}{\partial u_2(s-j)} & \cdots & \frac{\partial f_2^*}{\partial u_n(s-j)}\\ \vdots & \vdots & \ddots & \vdots\\ \frac{\partial f_n^*}{\partial u_1(s-j)} & \frac{\partial f_n^*}{\partial u_2(s-j)} & \cdots & \frac{\partial f_n^*}{\partial u_n(s-j)}\end{bmatrix}\end{aligned} \tag{A3}$$

where $\frac{\partial\mathbf{f}^*}{\partial\mathbf{v}(s-i)}$ and $\frac{\partial\mathbf{f}^*}{\partial\mathbf{u}(s-j)}$ denotes the mean value of the Jacobian Matrix of $\mathbf{f}(\cdot)$ with respect to all variables at certain point between

$$[\mathbf{v}^{\mathrm{T}}(s),\cdots,\mathbf{v}^{\mathrm{T}}(s-p_v),\mathbf{u}^{\mathrm{T}}(s),\cdots,\mathbf{u}^{\mathrm{T}}(s-p_u)]^{\mathrm{T}} \tag{A4}$$

and

$$[\mathbf{v}^{\mathrm{T}}(s-1),\cdots,\mathbf{v}^{\mathrm{T}}(s-p_v-1),\mathbf{u}^{\mathrm{T}}(s-1),\cdots,\mathbf{u}^{\mathrm{T}}(s-p_u-1)]^{\mathrm{T}} \tag{A5}$$

Denote

$$\begin{aligned}\psi(s) = &\frac{\partial \mathbf{f}^*}{\partial \mathbf{v}(s-L_v)}\Delta\mathbf{v}(s-L_v)+\ldots+\frac{\partial \mathbf{f}^*}{\partial \mathbf{v}(s-p_v)}\Delta\mathbf{v}(s-p_v)\\ &+\frac{\partial \mathbf{f}^*}{\partial \mathbf{u}(s-L_u)}\Delta\mathbf{u}(s-L_u)+\ldots+\frac{\partial \mathbf{f}^*}{\partial \mathbf{u}(s-p_u)}\Delta\mathbf{u}(s-p_u)\end{aligned} \tag{A6}$$

Noting that $\psi(s)$ is a bounded numerical value vector in nature at a given time k, and considering the following pure numerical data relationship matrix equation with a variable $\jmath(s)$ for every fixed time instant k.

$$\begin{aligned}\psi(s) =&\jmath(s)[\Delta\mathbf{v}^{\mathrm{T}}(s),\cdots,\Delta\mathbf{v}^{\mathrm{T}}(s-L_v+1),\Delta\mathbf{u}^{\mathrm{T}}(s),\cdots,\Delta\mathbf{u}^{\mathrm{T}}(s-L_u+1)]^{\mathrm{T}}\\ =&\jmath(s)\Delta\mathbf{H}(s)\end{aligned} \tag{A7}$$

At least one solution matrix $\jmath^*(s)$ must exist for (60) due to $\|\Delta\mathbf{H}(s)\| \neq 0$. Denoting

$$\mathbf{\Phi}(s) = [\frac{\partial \mathbf{f}^*}{\partial \mathbf{v}(s)},\cdots,\frac{\partial \mathbf{f}^*}{\partial \mathbf{v}v(s-L_v+1)},\frac{\partial \mathbf{f}^*}{\partial \mathbf{u}(s)},\cdots,\frac{\partial \mathbf{f}^*}{\partial \mathbf{u}(s-L_u+1)}]^T+\jmath^*(s) \tag{A8}$$

this yields the direct result of the FFDL data model (4).

By the FFDL data model (4) and Assumption 2, one has

$$\|\Delta\mathbf{v}(s+1)\| = \left\|\mathbf{\Phi}^{\mathrm{T}}(s)\Delta\mathbf{H}(s)\right\| \leq b\|\Delta\mathbf{H}(s)\| \tag{A9}$$

for any k and $\|\mathbf{\Phi}(s)\| \leq b$. From the above-mentioned inequality, we can see that if any element matrix of $\mathbf{\Phi}(s)$ is unbounded, it would violate the inequality (62). Therefore, the boundedness of $\mathbf{\Phi}(s)$ is guaranteed for any k.

References

1. Qu, S.; Xia, X.; Zhang, J. Dynamical behaviors of an Euler discretized sliding mode control systems. *IEEE Trans Autom. Control* **2014**, *59*, 2525–2529.
2. Xu, J.; Sui, Z.; Wang, W.; Xu, F. An Adaptive Discrete Integral Terminal Sliding Mode Control Method for a Two-Joint Manipulator. *Processes* **2024**, *12*, 1106. [CrossRef]
3. Zheng, Y.; Zheng, J.; Shao, K.; Zhao, H.; Xie, H.; Wang, H. Adaptive Trajectory Tracking Control for Nonholonomic Wheeled Mobile Robots: A Barrier Function Sliding Mode Approach. *IEEE/CAA J. Autom. Sin.* **2024**, *11*, 1007–1021.
4. Xue, J.Z.; Zhao, T.; Bu, N.; Chen, X.-L.; Zhang, B. Speed tracking control of high-speed train based on adaptive control and linear active disturbance rejection control. *Trans. Inst. Meas. Control* **2023**, *45*, 1896–1909.
5. Zhou, L.; Li, Z.; Yang, H.; Tan, C.; Fu, Y. Adaptive terminal sliding mode control for high-speed EMU: A MIMO data-driven approach. *IEEE Trans. Autom. Sci. Eng.* **2024**, 1–14. *in press*. [CrossRef]
6. Xu, J.; Xu, F.; Wang, Y.; Sui, Z. An Improved Model-Free Adaptive Nonlinear Control and Its Automatic Application. *Appl. Sci.* **2023**, *13*, 9145. [CrossRef]
7. Xu, F.; Sui, Z.; Wang, Y.; Xu, J. An Improved Data-Driven Integral Sliding-Mode Control and Its Automation Application. *Appl. Sci.* **2023**, *13*, 13094. [CrossRef]
8. Ma, H.; Wu, J.; Xiong, Z. Discrete-time sliding-mode control with improved quasi-sliding-mode domain. *IEEE Trans. Ind. Electron.* **2016**, *63*, 6292–6304.
9. Yu, X.; Kaynak, O. Sliding-mode control with soft computing: A survey. *IEEE Trans. Ind. Electron.* **2009**, *56*, 3275–3285.
10. Corradini, M.L.; Ippoliti, G.; Longhi, S.; Orlando, G. A quasi-sliding mode approach for robust control and speed estimation of PM synchronous motors. *IEEE Trans. Ind. Electron.* **2012**, *59*, 1096–1104.
11. Veselic, B.; Perunicic-Drazenovic, B.; Milosavljevic, C. Improved discrete-time sliding-mode position control using Euler velocity estimation. *IEEE Trans. Ind. Electron.* **2010**, *57*, 3840–3847.
12. Mehta, A.J.; Bandyopadhyay, B.; Inoue, A. Reduced-order observer design for servo system using duality to discrete-time sliding-surface design. *IEEE Trans. Ind. Electron.* **2010**, *57*, 3793–3800.
13. Shoja Majidabad, S.; Toosian Shandiz, H. Discrete-time based sliding-mode control of robot manipulators. *Int. J. Intell. Comput. Cybern.* **2012**, *5*, 340–358.
14. Qu, S.; Xia, X.; Zhang, J. Dynamics of discrete-time sliding-mode-control uncertain systems with a disturbance compensator. *IEEE Trans. Ind. Electron.* **2014**, *61*, 3502–3510.

15. Xu, Q.; Li, Y. Model predictive discrete-time sliding mode control of a nanopositioning piezostage without modeling hysteresis. *IEEE Trans. Control Syst. Technol.* **2012**, *20*, 983–994.
16. Xu, J.X.; Abidi, K. Discrete-time output integral sliding-mode control for a piezomotor-driven linear motion stage. *IEEE Trans. Ind. Electron.* **2008**, *55*, 3917–3926.
17. Xu, Q.; Li, Y. Micro-/nanopositioning using model predictive output integral discrete sliding mode control. *IEEE Trans. Ind. Electron.* **2012**, *59*, 1161–1170.
18. Xu, Q. Digital integral terminal sliding mode predictive control of piezoelectric-driven motion system. *IEEE Trans. Ind. Electron.* **2016**, *63*, 3976–3984.
19. Li, Z.Q.; Tang, B.W.; Yang, H.; Huang, L.J. Distributed global fast terminal Sliding model control strategy for high-speed train. *Railw. J.* **2023**, *45*, 41–50.
20. Lu, X.J.; Wang, X.J.; Dong, H.Y.; Dong, H.Y.; Ma, B.F. Research on sliding mode Predictive control for energy saving operation of high-speed trains. *Control Eng. China* **2016**, *23*, 389–393.
21. Hou, Z.S.; Jin, S.T. *Model Free Adaptive Control-Theory and Applications*; CRC Press: Boca Raton, FL, USA, 2013; pp. 45–118.
22. Wang, W.H.; Hou, Z.S. New adaptive quasi-sliding mode control for nonlinear discrete-time systems. *J. Syst. Eng. Electron.* **2008**, *19*, 154–160.
23. Hou, Z.S.; Wang, W.H.; Jin, S.T. Adaptive quasi-sliding-mode control for a class of nonlinear discrete-time systems. *Control Theory Appl.* **2009**, *26*, 505–509.
24. Wang, X.F.; Li, X.; Wang, J.H. Active interaction exercise control of exoskeleton upper limb rehabilitation robot using model-free adaptive methods. *Acta Autom. Sin.* **2016**, *42*, 1899–1914.
25. Bu, X.; Hou, Z.; Yu, F.; Fu, Z. Model free adaptive control with disturbance observer. *J. Control Eng. Appl. Inform.* **2012**, *14*, 42–49.
26. Weng, Y.P.; Gao, X.W.; Lv, M.Y. Improved model-free adaptive control for a class of non-affine nonlinear discrete systems. *Control Decis.* **2014**, *29*, 2226–2234.
27. He, D.-K.; Gao, F.-X.; Yang, L.; Wu, W. Improved adaptive quasi-sliding mode decoupling control for a class of unknown MIMO nonlinear discrete-time systems. *Control Decis.* **2016**, *31*, 783–789.
28. Wang, H.J. *Research on Model-Free Adaptive Fault-Tolerant Control of Subway Trains*; Beijing Jiaotong University: Beijing, China, 2020.
29. Li, Z.Q.; Zhou, L.; Yang, H. Data driven model-free adaptive control method for high-speed EMUs. *Acta Autom. Sin.* **2023**, *49*, 437–447.
30. Hao, L.Y.; Yang, S.; Liu, D. Model-free adaptive sliding mode con trol for discrete-time nonlinear systems with sensor fault and prescribed performance. In Proceedings of the IEEE 11th Data Driven Control and Learning Systems Conference (DDCLS), Chengdu, China, 3–5 August 2022; pp. 1395–1400.
31. Incremona, G.P.; Ferrara, A.; Magni, L. MPC for robot manipulators with integral sliding modes generation. *IEEE/ASME Trans. Mechatron ICS* **2017**, *22*, 1299–1307.
32. Zhu, Z.; Zhu, Z. Quasi-sliding mode model-free adaptive control for a class of second-order nonlinear systems. *Control Decis.* **2024**, *39*, 2663–2670. [CrossRef]
33. Li, Z.; Zhang, Z.; Wang, K.; Sun, H. Improved adaptive sliding mode auto-disturbance rejection control for PMLSM based on model free theory. *Electr. Mach. Control* **2024**, *28*, 142–151.
34. Wang, Y.; Hou, M. Model-free adaptive integral terminal sliding mode predictive control for a class of discrete-time nonlinear systems. *ISA Trans.* **2019**, *93*, 209–217.
35. Chi, R.; Hui, Y.; Huang, B.; Hou, Z. Active disturbance rejection con trol for nonaffined globally Lipschitz nonlinear discrete-time systems. *IEEE Trans. Autom. Control* **2021**, *66*, 5955–5967.
36. Huang, X.; Dong, Z.; Zhang, F.; Zhang, L. Discrete-time extended state observer-based model-free adaptive sliding mode control with prescribed performance. *Int. J. Robust Nonlinear Control* **2022**, *32*, 4816–4842.
37. Zhou, L.; Li, Z.; Yang, H.; Fu, Y.; Yan, Y. Data-driven model-free adaptive sliding mode control based on FFDL for electric multiple units. *Appl. Sci.* **2022**, *12*, 10983.
38. Yan, S. *Collaborative Optimization Design Method and Specialized Software Development of Vertical and Horizontal Stability of Forklift*; Hefei University of Technology: Hefei, China, 2022.
39. Xu, J.; Sui, Z.; Xu, F.; Wang, Y. A Novel Model-Free Adaptive Proportional–Integral–Derivative Control Method for Speed-Tracking Systems of Electric Balanced Forklifts. *Appl. Sci.* **2023**, *13*, 12816. [CrossRef]
40. Olejnik, P.; Awrejcewicz, J. Low-Speed Voltage-Input Tracking Control of a DC-Motor Numerically Modelled by a Dynamical System with Stick-Slip Friction. *Differ. Eq. Dyn. Syst.* **2013**, *21*, 3–13. [CrossRef]
41. Utkin, V.I. Sliding mode control design principles and applications to electric drives. *IEEE Trans. Ind. Electron.* **1993**, *40*, 23–36. [CrossRef]